Topology optimization for mass transfer enhancement in open thermochemical energy storage reactors

Humbert, Gabriele; Sciacovelli, Adriano

DOI:
10.1016/j.est.2023.107132

Document Version
Publisher's PDF, also known as Version of record

Citation for published version (Harvard):
Humbert, G & Sciacovelli, A 2023, 'Topology optimization for mass transfer enhancement in open thermochemical energy storage reactors', *Journal of Energy Storage*, vol. 64, 107132. https://doi.org/10.1016/j.est.2023.107132

Journal of Energy Storage 64 (2023) 107132

Contents lists available at ScienceDirect

Journal of Energy Storage

journal homepage: www.elsevier.com/locate/est

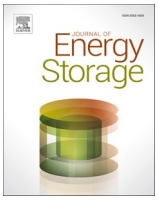

Research papers

Topology optimization for mass transfer enhancement in open thermochemical energy storage reactors

Gabriele Humbert, Adriano Sciacovelli *

Birmingham Centre for Energy Storage, School of Chemical Engineering, University of Birmingham, UK

ARTICLE INFO

Keywords:
Thermal energy storage
Thermochemical energy storage
Heat and mass transfer enhancement
Numerical methods
Topology optimization
Decarbonization

ABSTRACT

The mass transfer enhancement in open system thermochemical energy storage is achieved in this work through the optimal design of flow channel geometries. Such flow channel geometries aim to maximize how gas reactants are distributed to the reactive sites and are derived from the topology optimization algorithm. Two reactor configurations are analyzed, namely sieve reactors and cylindrical reactors, and the performance of the generated designs are compared with literature benchmarks. Tentacular flow channel geometries emerged, with the flow channels elongating in the reactive bed without directly connecting the inlet and outlet interfaces. In the instance of a fixed time, a +757.8 % increase in the amount of discharged energy is obtained compared to literature solutions. Besides, the optimal geometrical features differ depending on the targeted performance metric. In particular, thinner channels are found to be favourable to increasing the amount of discharged exergy compared to discharged energy. Overall, the emerging design trends define new enhancement pathways for the performance improvement of open system thermochemical energy storage reactors and significantly contribute to the technology advancement.

1. Introduction

Thermochemical energy storage (TCS) presents the advantages of larger energy density and nearly null heat losses, and it is thus considered particularly attractive for long-term thermal energy storage [1]. Several promising results about the use of TCS reactors in existing energy systems have been published in the literature [2]. However, such results exhibit measured performance to significantly differ from the theoretical maximum values. For most of the tested TCS prototypes, a ≈50 % reduction between the reactor energy density and storage material energy density was reported [3,4]. Such a performance gap is often attributed by researchers to the ineffective heat and mass transfer in the reactive beds [5]. In particular, given the complex multiphysics phenomena occurring in TCS reactive beds, the configuration of efficient reactor geometries is a challenging task.

This work deals with TCS reactors operated in the open system mode and employing gas/solid reactions. For this type of system operation, air at ambient pressure is typically adopted to transport water vapour through a porous thermochemical material (TCM) [6]. An overview of the main geometrical configurations adopted in the literature is reported in Fig. 1. Each reported configuration can be considered modular, thus a single module is depicted to represent the reactor concept. Due to their ease of manufacturability, cylindrical reactors are the most investigated configurations, especially for laboratory-scale testing [7–9]. However, for scaled-up designs entailing longer units, the required large pressure drops make such configurations unattractive [10].

Nonetheless, the mass transfer limitation can be attenuated by air diffusers [11]. In particular, Michel et al. [12] measured the use of a gas diffuser to lead to an effective permeability increase of up to +70 % compared to a reactive bed without diffusers. Benefits were also reported in terms of specific power, +12.5 %. With the same finality to mitigate the mass transfer resistance effects, radial reactors have been proposed and investigated by Krönauera et al. [13] for a 14 tons storage adopting zeolite. Promising results were reported, although the flow misdistribution through the reactive bed precluded the desired power output, indicating the need for a more in-deep analysis of the effective configuration of radial TCS reactors. The testing of large-scale reactors was also successful in the instance of rectangular configurations [14]. For example, Michel et al. [3] tested a 105 kWh storage unit employing $SrBr_2{\cdot}6H_2O$ in the context of long-term storage for domestic applications. The rectangular configuration was adopted to ensure a simple and cheap storage unit, with the mass transfer limitations mitigated by selecting a small reactive bed height. In recent years, Li et al. [15]

* Corresponding author.
E-mail address: a.sciacovelli@bham.ac.uk (A. Sciacovelli).

https://doi.org/10.1016/j.est.2023.107132
Received 30 September 2022; Received in revised form 7 February 2023; Accepted 10 March 2023
Available online 30 March 2023

Nomenclature

Acronyms

FC	Flow channels
HE	Heat Exchanger
TCM	Thermochemical material
TCS	Thermochemical storage
TES	Thermal energy storage
TO	Topology optimization

Symbols

$\dot{m}_{LF}$	Mass sink constant, [mol/m^3/s]
ΔH	Enthalpy of reaction, [J/mol]
ΔT	Temperature lift, [K]
c	Vapour molar concentration, [mol/m^3]
c_p	Specific heat, [J/kg/K]
D	Diffusion coefficient, [m^2/s]
E	Reactor energy density, [kWh/m^3]
K	Permeability, [1/m^2]
k_{cin}	Reaction kinetics, [1/s]
k_{cin}	Kinetic constant, [1/s]
L	Characteristic length, [m]
n_s	TCM molar density, [mol/m^3]
p	Air pressure, [Pa]
P	Reactor power output per unit length, [W/m]
p_v	Vapour pressure, [Pa]
$p_{v,\,eq}$	Equilibrium pressure, [Pa]
q	Convexity factor, [–]
s	Design variable, [–]
t	Time, [s]
T	Temperature, [K]
u	Velocity field, [m/s]
α	Reaction advancement, [–]
α_b	Brinkman term, [–]
γ	Stoichiometric coefficient, [–]
Γ	Boundary, [m]
λ	Thermal conductivity, [W/m/K]
μ	Dynamic viscosity, [Pa·s]
ρ	Density, [kg/m^3]
Ω	Domain, [m^2]

Subscripts

eff	Volumetric effective

proposed and numerically investigated the use of sieve reactors. Besides enhancing the overall mass transfer, this reactor configuration also ensures separate beds, effectively mitigating deliquescence phenomena.

Furthermore, numerical studies were conducted aimed at improving the reactor performance through the variation of geometrical variables. Malley-Ernewein et al. [16] studied a rectangular reactor using constructal theory [17]. The results exhibited an increase in the number of salt layers to benefit the overall system performance. Besides, a height over width ratio of 1.6 was identified as optimal. With similar finalities, Hawwash et al. [18] compared the performance of cylindrical reactors and truncated cones with variable aspect ratios, defined as the ratio between outlet and inlet areas. A fixed amount of storage material was considered for all the investigated designs. Shorter charging times were encountered for small aspect ratios at the expense of an increased pressure drop. In the instance of a sieve reactor employing hexahydrate magnesium chloride, Chen et al. [19] analyzed the effect of the main geometrical parameters on the reactor performance. A final configuration adopting six sieve plates and a ratio between plate length and thickness of 30 was selected.

Despite the benefits led by the numerical studies reported above, the adopted design approaches were based on the heuristic selection of geometrical parameters, which ultimately constrained the final design to the ones depicted in Fig. 1. In this work, the limitation posed by selecting a constrained design space is broken by the use of the topology optimization algorithm. Topology optimization (TO) is indeed a form-finding methodology that does not require any initial guess for the layout, ultimately ensuring matchless freedom in generating optimal designs [20].

However, the high complexity of the TO algorithm often prevents its direct application in real engineering problems [21,22]. To overcome this barrier, a multi-step optimization approach is adopted, similar to what was initially proposed by Yaji et al. [23]. The approach aims at indirectly solving complex topology optimization problems. The original problem is indeed addressed by defining the topological design optimization of a pseudo problem and a consecutive performance assessment. The pseudo problem optimization is based on a simplified numerical model and aims at defining a series of TO-based flow channel geometries that effectively distribute gas reactants to reactive sites. Thus, a full numerical model is used to assess the generated design candidates and to quantify the performance enhancement obtained compared to literature designs. In such a way, a tailored and highly replicable design strategy is proposed to generate high-performing TCS reactors. Overall, the adopted design approach alleviates the topology optimization problem from the complexity of the full physical problem description but still allows for generating design guidelines for real-world devices.

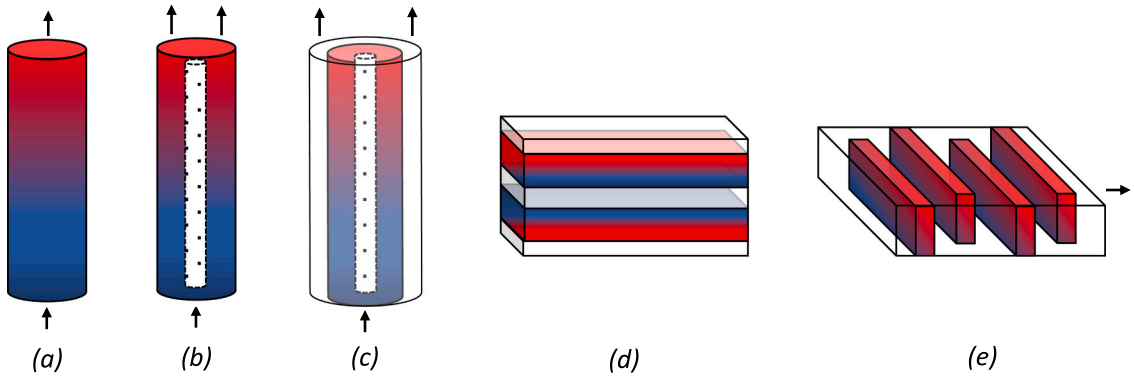

Fig. 1. Simplified schematics for the open system TCS reactor configurations adopted in the literature: (a) cylindrical reactor, (b) cylindrical rector employing a diffuser, (c) radial reactor, (d) rectangular reactor, (e) sieve reactor.

1.1. Novelty and contributions

This work deals with the need for mass transfer enhancement in open system TCS reactors. Mass transfer is enhanced through the generation of flow channel geometries which effectively distribute gas reactants to the reactive sites. Uniquely to this work, topology optimization is adopted for the non-heuristic design of such flow channel geometries. That is, unlike previous studies on the effective design of open system TCS reactors, the optimal geometries are obtained in this work with matchless design freedom. The performance of the optimized designs is quantified against literature benchmarks to assess the benefits led by the proposed optimization approach fairly. Furthermore, a comprehensive analysis of the emerging design trends is carried out to identify which geometrical features lead to TCS reactors with superior performance. Overall, the results presented in this work define new enhancement pathways for the performance maximization of open system TCS reactors and ultimately contribute to technology advancement.

2. TCS reactor configurations

TCS reactors operated in the open system mode are investigated. An open system reactor exchanges mass and energy with the environment and consists of a single vessel containing the solid TCM crossed by moist air at atmospheric pressure, as shown in Fig. 2. During the charging process, the airflow is heated up from a heat source and circulated in the reactive bed in such a way that TCM dehydration occurs. On the other hand, cold and humid air from the ambient flows through the reactor during discharge and is heated up by the exothermic process. The hot airflow exiting the reactor is thus circulated to and heat exchanger to deliver energy to the user.

This work focuses on the design optimization of open reactor, with the influence of the auxiliary components approximated through the choice of suitable boundary conditions. Two reactor configurations are analyzed. Specifically, a sieve reactor, Fig. 3 (a), and a cylindrical reactor, Fig. 3 (b). Both configurations are depicted employing heuristic flow channel geometries from the literature. Both configurations consist of modular storage units where a series of identical TCS reactors can be placed in parallel [19]. The reactors operate at ambient pressure, and the sorbate, H_2O, is transported by an airflow. The airflow is circulated by means of a fan into the storage units and crosses the porous TCM [24]. In such a way, the airflow concurrently constitutes the reactants carrier and the heat transfer fluid. Identical operating conditions can be assumed for each TCS reactor module in the storage unit, and thus the study of a single module can be performed in order to enhance the whole system's performance [24,25].

Concerning sieve reactors, Fig. 2 (a), the reactor configuration proposed by Chen et al. [18] was considered as benchmark design. The

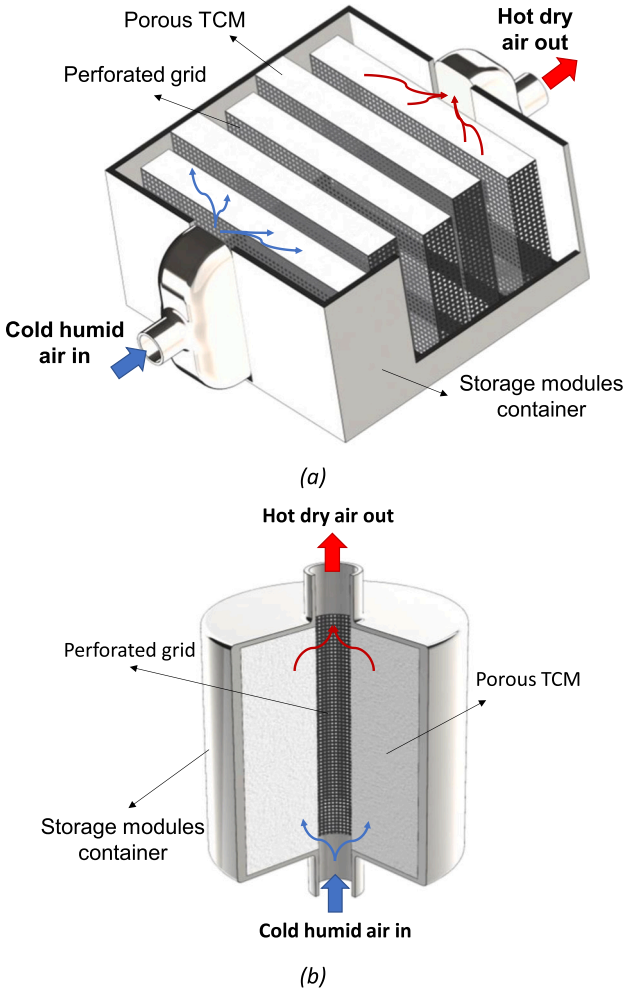

Fig. 3. Schematic of the TCS reactor configurations under investigation: (a) sieve reactor adapted from Chen et al. [19], (b) cylindrical reactor adapted from Aydin et al. [11].

design presented a 60 cm length and 30 cm width. A serpentine flow channel geometry was employed to distribute moist air in six rectangular domains. Assuming a 1 m height, these domains were thus filled with 35.6 l of $MgCl_2{\cdot}6H_2O$ and numerically tested to serve low-temperature applications. As a benchmark design for the cylindrical configuration, the design proposed by Aydin et al. [11] was selected. A

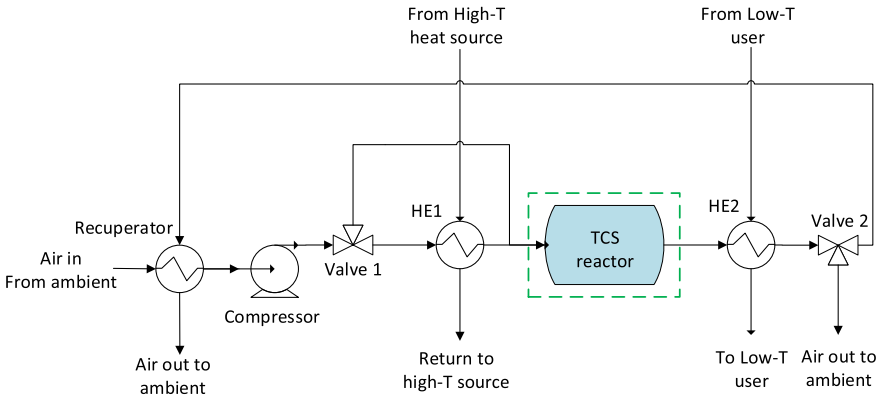

Fig. 2. Schematic of a TCS system operated in the open mode, partially adapted from Scapino et al. [2]. During dehydration/desorption, valve 1 directs the airflow to HE1 to be heated up by a high-temperature heat source, e.g. solar collector. During hydration/sorption, HE1 is bypassed, while HE2 is used to transfer heat to the user. A recuperator unit is often adopted to increase the system coefficient of performance.

straight inner diffuser with a 0.05 m diameter was used to distribute the airflow in the surrounding TCM region. The unit presented a storage volume of 29.4 l and was tested for typical conditions for domestic heating applications and multiple composite TCMs, leading to measured heat storage capacities in the range of 31.8 to 100.5 kWh/m^3.

The investigation carried out in this work was conducted in the context of domestic heating applications. The system's thermodynamic constraints were derived assuming the TCS charging process to be operated by a solar collector unit at 80 °C [12] and the discharging process to be operated at the conditions of 25 °C with a partial vapour pressure of 998 Pa. These discharging conditions were selected in the range of moist air conditions encountered by a seasonal storage process [26] and in agreement with the conditions adopted in the experimental setup investigated by Michel et al. [3]. For the resulting thermodynamics constraints, the most suitable TCM was selected according to the results reported by N'Tsoukpoe et al. [27]. In this study, a set of 125 salt hydrates candidates were screened and $SrBr_2{\cdot}6H_2O$ was identified as the most promising candidate due to its large energy density, non-toxicity and suitable hydration and dehydration curves. A possible concern for this material selection relates to the high specific material cost of strontium bromide [28]. Nonetheless, the production process of this salt on a large scale is not yet optimized, and costs are predicted to decrease with the increase in its application, as investigated by Gilles et al. [29]. Furthermore, several successful experimental studies adopting $SrBr_2{\cdot}6H_2O$ as storage material have been reported in the literature [30]. Hence, the considered storage system relies on the heat generated and retrieved by the following reaction:

$$SrBr_2{\cdot}1H_2O + 5\,H_2O \leftrightarrow SrBr_2{\cdot}6H_2O + \Delta H \tag{2.1}$$

where $SrBr_2{\cdot}1H_2O$ and $SrBr_2{\cdot}6H_2O$ are, respectively, the monohydrated and hexahydrated states, while the reactive gas is water. The term $\Delta H = 3.37 \bullet 10^5\ J/mol_{TCM}$ represents the reaction enthalpy. The equilibrium conditions for this solid/gas reaction follow the Clausius-Clapeyron relation, which is obtained assuming that the free Gibbs energy of the transformation is null at the thermodynamic equilibrium [24].

The hydrated and dehydrated salt thermo-physical properties are reported in Table 1. The analysis solely focused on the TCM hydration as this controls the discharging process and ultimately governs the amount of heat retrieved from the TCS system [26]. According to the properties reported in Table 1, the energy storage density of the system, accounting for the void volumes in the porous TCM, is 389.6 kWh/m^3. Assuming a fully charged unit, such a value constitutes thus the maximum amount of energy that can be retrieved by the reactor per unit of volume.

Table 1
Thermophysical properties for the selected TCM: the subscript 0 refers to the dehydrated material, $SrBr_2{\cdot}1H_2O$, while the subscript 1 refers to the hydrated material, $SrBr_2{\cdot}6H_2O$ [24].

Property	Value	Unit
ΔH	$3.37 \bullet 10^5$	J/mol$_{TCM}$
Δs	875	J/mol$_{TCM}$/K
γ	5	–
λ_{TCM}	1	W/m/K
$\varepsilon_{TCM,0}$	0.68	–
$\varepsilon_{TCM,1}$	0.38	–
$K_{TCM,0}$	$1.0 \bullet 10^{-10}$	m^2
$K_{TCM,1}$	$5.0 \bullet 10^{-12}$	m^2
$M_{TCM,0}$	266	g/mol$_{TCM}$
$M_{TCM,1}$	356	g/mol$_{TCM}$
$c_{p,TCM,0}$	456	J/kg/K
$c_{p,TCM,1}$	968	J/kg/K
$\rho_{TCM,0}$	3481	kg/m^3
$\rho_{TCM,1}$	2390	kg/m^3

3. Optimization approach and numerical methods

3.1. Optimization approach

The optimization approach adopted for the performance enhancement of open system TCS reactors is reported in Fig. 4. First, a representative unit is identified for each one of the investigated reactor configurations, as detailed in Section 3.2. Thus, the design problem for the efficient configuration of flow channel geometries is divided into two subproblems: topological design optimization and performance assessment. The topological design optimization makes use of a highly solvable numerical model, referred to as pseudo model, which decreases the nonlinearities of the original problem and can be thus easily coupled to the topology optimization algorithm. Besides, artificial design parameters, namely the seeding parameters, are incorporated into the pseudo problem optimization in such a way that various topology-optimized candidates are generated. The selection of proper seeding parameters is crucial to generating various design patterns. In this work, the seeding parameters were selected to represent physical parameters of the targeted problem in order to guarantee meaningful results interpretation and to guide the selection of the seeding parameter values. The multiple topology-optimized candidates are thus reconstructed to generate CAD designs whose performance is then evaluated using a validated numerical model, referred to as full model. Finally, the benefits led by the proposed optimization framework are quantified by comparison with the selected literature benchmarks [19].

3.2. Mathematical models

3.2.1. Pseudo model

The aim of the flow channel design is to effectively distribute reactants in the porous region in such a way that TCM hydration can occur. To such an extent, the pseudo model is constructed to describe an isothermal reactor in steady-state conditions [31]. Besides, the governing equations are expressed to allow for a density-based description of the distributed materials, as typically done in fluid-based problems [32,33]. The density-based description adopts a continuous scalar indicator function, s, for the switching between material phases [34]. Such a scalar indicator becomes the control variable of the optimization problem. Nevertheless, artificial differentiable laws need to be formulated to express the density-property relations, as detailed in Section 3.3.

In the instance of the sieve reactor configuration, three-dimensional effects can be neglected, and heat and mass transfer was assumed to occur in the horizontal plane [19]. Following this assumption, a 2D planar ground domain was adopted for the analysis of the performance maximization of the TCS reactor in Section 3, as depicted in Fig. 5. Similarly, an axisymmetric assumption was made for the cylindrical reactor [35], which ultimately alleviates the analysis from the need for 3D simulations.

In the framework of the pseudo model, a convective diffusive equation was adopted to predict the reactants concentration distribution, while the Darcy law was used to describe the momentum conservation:

$$\nabla \bullet \mathbf{u} = 0 \tag{3.1}$$

$$\mathbf{u} = -\frac{1}{\alpha_b(s)} \nabla \bullet p \tag{3.2}$$

$$\mathbf{u}\nabla c = D\nabla^2 c - \dot{m}(s)\left(\frac{p_v - p_{eq}\,(T_0)}{p_{v,in}}\right) \tag{3.3}$$

where $\boldsymbol{u}$ is the velocity field, c is the vapour molar concentration, p is the airflow pressure, p_v is the relative vapour pressure, and p_{eq} is the equilibrium pressure for the TCM hydration. The terms $\alpha_b(s)$ and $\dot{m}_{LF}(s)$ are the design-dependent inverse permeability and mass sink terms,

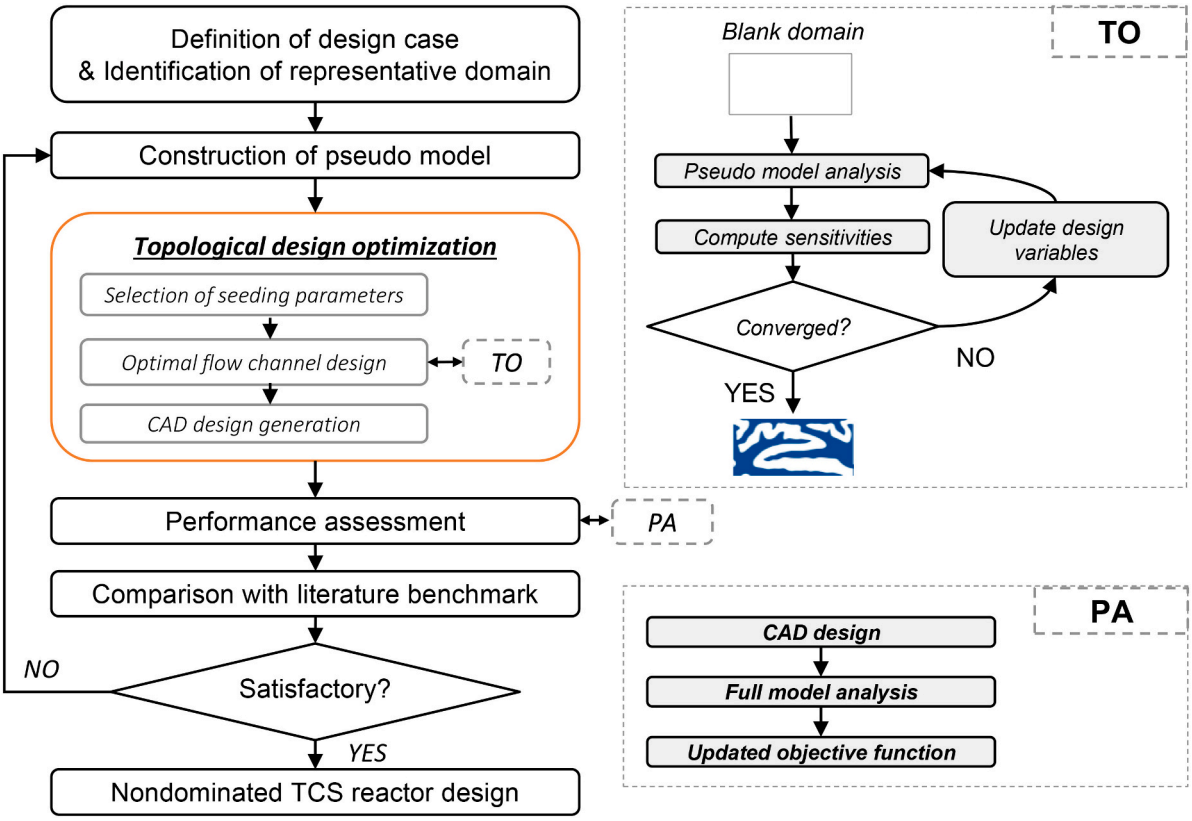

Fig. 4. Optimization approach adopted for the mass transfer intensification in open system TCS reactors.

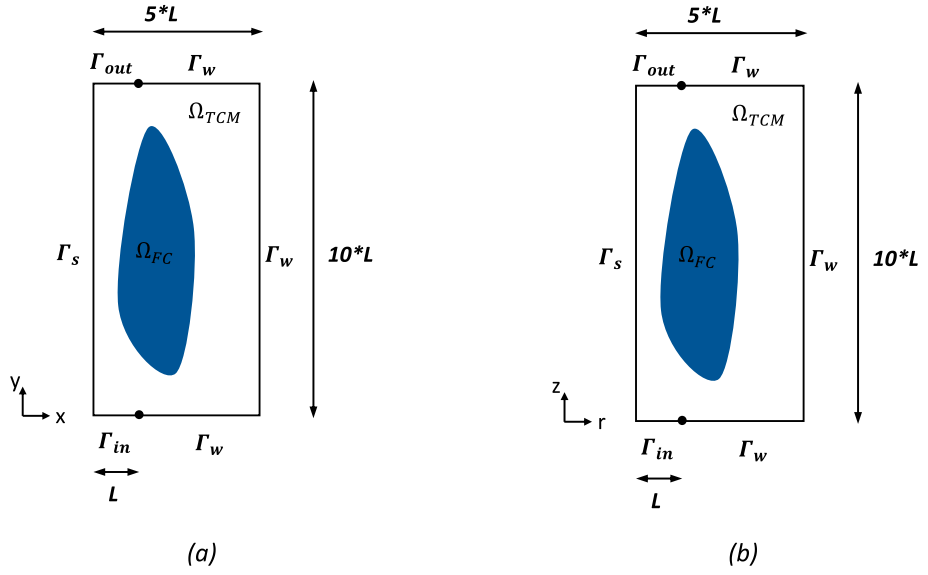

Fig. 5. Ground domains for the optimization problems: (a) sieve reactor configuration; (b) cylindrical reactor configuration.

respectively. The material interpolation strategies were formulated in such a way to recover the material properties in the TCM domain, Ω_{TCM}, and in the flow channel domain, Ω_{FC}, in the following way:

$$s = \begin{cases} 0 \; in \; \Omega_{TCM} \\ 1 \; in \; \Omega_{FC} \end{cases} \tag{3.4}$$

The ground domain, $\Omega_d = \Omega_{TCM} \bigcup \Omega_{FC}$, adopted for the generation of TO-based candidates is depicted in Fig. 5. The same key geometrical dimensions were adopted for both the reactor configurations under investigation. The distinction between the two cases was made by the use of Cartesian coordinates in the instance of sieve reactor configuration [25] and cylindrical coordinates in the instance of cylindrical reactor configuration [35].

The parameter L was fixed as *5 cm* to obtain reactor volumes in agreement with large scale prototypes tested in the literature [3,36]. Ambient pressure was prescribed at the outlet interface, Γ_{out}, while a *1000 Pa* pressure difference was imposed between the inlet and outlet interfaces. A limited pressure difference is indeed desired to limit the

energy required for the auxiliary components, and the imposed pressure difference value was selected in agreement with the suitable range identified in [24]. The inlet partial vapour pressure, $p_{v,\ in}$, was imposed at the inlet interface Γ_{in}. Null flux was instead prescribed at the wall and symmetry interfaces, Γ_w and Γ_s respectively. A quadrilateral mesh was adopted, with an element size, h_{el}, equal to $L/5$.

In agreement with the selected dimensions, a reactor volume of 250 l was considered for the sieve reactor configurations (1.0 m height), while a reactor volume of 98.4 l was considered for the cylindrical configurations. The benchmark designs were scaled-up to match these reactor volumes and, thus, ensure fair comparability.

3.2.2. Full model

A full numerical model was implemented to accurately describe the heat and mass transfer mechanisms in the reactive bed and generated flow channel designs. The mass conservation for the vapour content in the porous TCM domain was described as follows:

$$\varepsilon\frac{\partial \mathrm{c}}{\partial t}+\boldsymbol{u}\nabla c+D\nabla^2 c=-\gamma \mathrm{n}_s\dot{\alpha} \tag{3.5}$$

where ε represents the bed porosity, γ is the stoichiometric coefficient, n_s is the TCM molar density and $\dot{\alpha}$ represents the rate of the reaction advancement. Eq. (3.5) was also adopted to describe the mass conservation in the flow channels domain, although here a null mass sink term, $-\gamma \mathrm{n}_s\dot{\alpha}=0$, was imposed, and an unitary porosity was considered [25]. The Darcy law described the momentum conservation in the porous domain [12,24]:

$$\mathbf{u}=-\frac{K}{\mu}\nabla p \tag{3.6}$$

where K indicates the permeability, μ the dynamic viscosity and p the airflow pressure. An artificial $K_{air}=1.0\bullet 10^{-8}\ \mathrm{m}^2$ was adopted in the FC domain to represent the nearly negligible mass transfer resistance compared to the porous TCM [24]. The energy conservation was written within the porous TCM domain as follows:

$$\left(\rho c_p\right)_{eff}\frac{\partial \mathrm{T}}{\partial t}+\rho c_p\boldsymbol{u}\bullet\nabla T+\nabla\bullet\left(\lambda_{eff}\nabla T\right)=n_s\dot{\alpha}\Delta H \tag{3.7}$$

where ρ is the density, c_p the specific heat, T the temperature, λ is the thermal conductivity, and ΔH is the enthalpy of reaction. The subscript *eff* refers instead to the effective values, which were calculated according to:

$$\left(\rho c_p\right)_{eff}=(1-\varepsilon)\rho_{TCM}\mathrm{c}_{p,TCM}+\varepsilon\rho_{air}\mathrm{c}_{p,air} \tag{3.8}$$

$$\lambda_{eff}=(1-\varepsilon)\lambda_{TCM}+\varepsilon\lambda_{air} \tag{3.9}$$

The energy equation was instead written in the flow channels as:

$$\left(\rho c_p\right)_{air}\frac{\partial \mathrm{T}}{\partial t}+\left(\rho c_p\right)_{air}\boldsymbol{u}\bullet\nabla T+\nabla\bullet\left(\lambda_{air}\nabla T\right)=0 \tag{3.10}$$

Finally, a 1st order reaction kinetics was adopted [37]:

$$\dot{\alpha}=k_{cin}\left(1-\alpha\right)\left(1-\frac{p_{eq}(T)}{p_v}\right) \tag{3.11}$$

where $k_{cin}=8\bullet 10^{-6}\ s^{-1}$ is the reaction kinetics constant and $p_{eq}(T)$ is the equilibrium pressure, assumed to follow the Clausius-Clapeyron relationship [3]:

$$ln\left(p_{eq}/p_0\right)=-\frac{\Delta H}{\gamma R T_{eq}}+\frac{\Delta \mathrm{s}}{\gamma R} \tag{3.12}$$

The partial vapour pressure was directly calculated from the molar concentration, assuming vapour as an ideal gas, $p_v=cR_{gas}T$ [12].

The material properties were interpolated between dehydrated and hydrated salt as a linear function of the reaction advancement [24], except for the material permeability, K_{TCM}, for which a $1/\alpha$ behaviour was assumed [12].

A constant temperature, $\mathrm{T_{in}}=25\ ^{\circ}\mathrm{C}$, and constant partial vapour pressure, $p_{v,in}=998$ Pa, were imposed at the inlet interface [3]. Besides, a reference pressure drop of 1000 Pa was adopted between the inlet and outlet interfaces, with the outlet interface considered at ambient pressure. In all the other boundaries, no flux conditions were imposed. The reactive bed is considered in thermal equilibrium with the inlet airflow at the initial time. That is, the initial temperature, $\mathrm{T_0}$, was set equal to the inlet airflow temperature. The initial partial vapour pressure, $\mathrm{p_{v,0}}$, was thus derived from Eq. (3.12) for the imposed initial temperature value.

The time-dependent study was solved in Comsol multiphysics environment [38] by adopting a backward differentiation formula with a time-adaptation scheme. Besides, an initial time step of 0.5 min and a maximum time step of 15 min were imposed. The inlet vapour pressure was ramped up from the initial equilibrium pressure to the selected inlet vapour pressure in a 30 min time range to smoothen the disequilibrium conditions during the initial stages of the hydration process [39]. Unstructured triangular meshes were adopted for the evaluation of each of the reconstructed designs. The minimum element size was set at $1.0\bullet 10^{-4}$, while the maximum element size was selected as $8.0\bullet 10^{-3}$ through a mesh convergence study, as depicted in Fig. 6. Besides, an example of unstructured mesh adopted for the performance assessment of one of the generated TO-based design candidates is shown in Fig. 7.

The full model described above was validated against the experimental data presented by Michel et al. [3]. Here, a rectangular reactor configuration with a 7.5 cm thickness was tested under realistic mid-season operating conditions. Fig. 8 shows the reaction advancement histories for the numerical and experimental data for three hydration cycles. A maximum mismatch below 3 % was achieved, demonstrating good reliability for the numerical predictions.

3.3. Topology optimization

The topology optimization algorithm was coupled with the pseudo model to generate multiple design candidates. The optimization problem considered in the analysis is the maximization of the reaction rate. We, therefore, introduce the following objective function:

$$\begin{cases} max\int_{\Omega_d}\dot{m}(s)\left(\dfrac{p_v-p_{eq}(T_0)}{p_{v,in}}\right) \\ 0\le s\le 1 \end{cases} \tag{3.13}$$

No volume constraints are necessary for the generation of optimal designs. In fact, while the generation of designs filled with TCM would lead to poor mass transfer performance, the use of purely FC in the design domain would entail a null reaction rate. The packing factor value, PF, is defined for each of the generated designs as follows:

$$PF=\frac{\int_{\Omega_{FC}}1\ dxdy}{\int_{\Omega_d}1\ dxdy}=\frac{\mathrm{V}_{FC}}{\mathrm{V}_{reactor}} \tag{3.14}$$

The packing factor value thus represents the amount of volume devoted to the flow channels over the reactor volume.

The adopted density-based approach requires the definition of fictitious design-dependent material properties. The body force and reaction rate term were thus defined as a function of the design variable, s, as follows:

$$\alpha_b(s)=\alpha_{b,TCM}+\left(\alpha_{b,FC}-\alpha_{b,TCM}\right)\frac{s(1+q)}{s+q} \tag{3.15}$$

$$\dot{m}(s)=\dot{m}_{LF}\ (1-s) \tag{3.16}$$

With $q=0.1$ representing the convexity of the interpolation scheme [22]. The body force terms for each of the distributed materials are

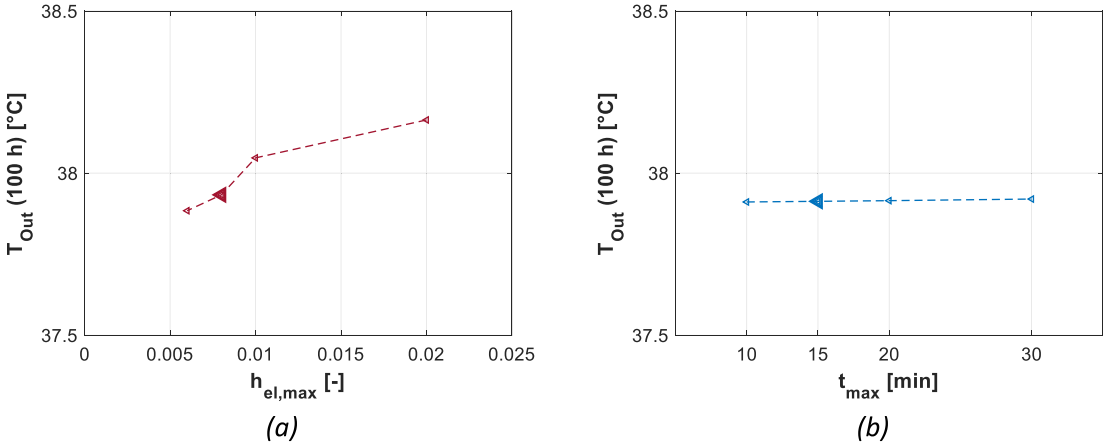

Fig. 6. Convergence studies: (a) influence of the mesh maximum element size; (b) influence of the maximum time-step.

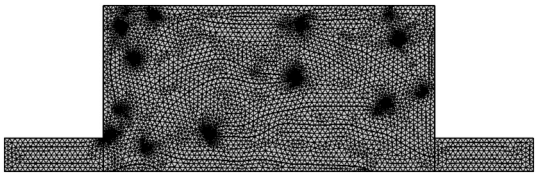

Fig. 7. Unstructured triangular mesh adopted for a TO-based design in the instance of sieve reactor configuration.

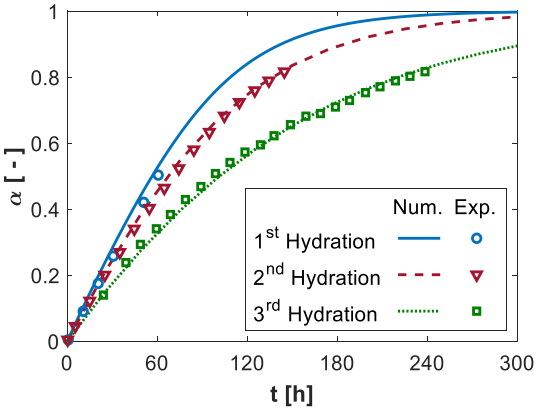

Fig. 8. Model validation against the data presented by Michel et al. [3].

defined as:

$$\alpha_{b,TCM} = \frac{K_{LF}}{\mu} \tag{3.17}$$

$$\alpha_{b,FC} = \frac{K_{air}}{\mu} \tag{3.18}$$

Seeding parameters were incorporated in the pseudo model for the generation of multiple layouts. Such seeding parameters were selected in this work to represent physical properties of the targeted design case. Specifically, the terms K_{LF} and $\dot{m}_{LF}$ were adopted as seeding parameters. The former directly refers to the TCM permeability. Given the TCM permeability value variation with the salt hydration level, two different K_{LF} values were considered. Specifically, the dehydrated and hydrated salt permeability. Concerning the $\dot{m}_{LF}$ parameter, this was thought of as the product of:

$$\dot{m}_{LF} = \frac{k_{cin}\gamma\ \mathrm{n}_s}{\varepsilon}(1-\alpha) \tag{3.19}$$

In agreement with the mass sink term expressed in Eq. (3.5). Thus, the term $\dot{m}_{LF}$ represents the mass sink constant for the constructed pseudo model, and its numerical values were directly derived from physical parameters. Again, two values were selected, accounting for different salt hydration levels. A first value assuming $\alpha = 0$, and a second seeding parameter level for $\alpha = 0.9$, as the assumption of a fully hydrated salt would result in null $\dot{m}_{LF}$. The selected seeding parameter values are reported in Table 2. The optimal designs were generated by combining the selected values to obtain a total of four designs for each of the configurations under investigation.

Filtering and regularization techniques were adopted to ensure mesh independence and avoid the checkboard effects in the emerging designs. The linear filter presented in [40] was considered, with a filtering radius equal to $h_{el}\bullet 1.1$ and a steepness projection parameter $\beta = 5.0$ [41]. The smoothing of the design variable was adjusted by the hyperbolic tangent projection operator, $\eta = 0.5$. The GCMMA was used as optimization routine to update the control variable [42], with a number of optimization iterations set at 200. Finally, the TO-based designs were reconstructed considering a cut-off parameter $s^* = 0.5$ [43].

3.4. Performance indicators

The performance assessment step was conducted on the design candidates generated by the topology optimization routine utilizing the full model presented in Section 3.2.2. Nonetheless, a series of performance indicators were defined to fairly compare the investigated geometries and to link geometrical features with the desired reactor performance [44]:

- The discharged energy, E_{t^*}:

$$E_{t^*} = \frac{\int_0^{t^*} \dot{m}_{air} c_{p,air}(T_{out} - T_{in})\, dt}{\mathrm{V}_{reactor}} \tag{3.20}$$

The discharged energy is referred to the reactor volume and is calculated as the time integral of the thermal energy transferred to the HTF. The term $\dot{m}_{air}$ represents the air mass flow rate, while the terms T_{out} and T_{in} refer to the air temperature at the outlet and inlet interfaces,

Table 2
Values selected for the seeding parameters.

Seeding parameter	Units	Level 1	Level 2
$\dot{m}_{LF}$	[mol/m^3/s]	0.3	0.1
K_{LF}	[m^2]	$1.0 \bullet 10^{-10}$	$5.0 \bullet 10^{-12}$

respectively. Finally, the term t^* represents the desired discharge time and was set equal to 200 h in the current investigation [3].

- The discharged exergy, Ex_{out,t^*}:

$$Ex_{out,t^*} = \frac{\int_0^{t^*} \dot{m}_{air} c_{p.air} \left(T_{out} - T_{in} - T_0 ln\left(\frac{T_{out}}{T_{in}}\right)\right) dt}{V_{reactor}} \quad (3.21)$$

The discharged exergy is defined as the time integral of the rate of exergy recovered by the HTF [45,46]. Higher discharged exergy values are desired to achieve a higher quality of discharged energy [47].

- The average temperature lift, ΔT_{t^*}:

$$\Delta T_{t^*} = \frac{\int_0^{t^*} T_{out} - T_{in}\, dt}{t^*} \quad (3.22)$$

The temperature lift is defined as the temperature difference between the outlet and inlet interface temperatures averaged over the desired discharge time.

- The peak of power output, P_{peak}:

$$P_{peak} = max\,(P) \quad (3.23)$$

The peak of power output is defined as the maximum thermal power output over the discharge history. The thermal power output, P, is defined as:

$$P = \frac{\dot{m}_{air} c_{p.air} (T_{out} - T_{in})}{V_{reactor}} \quad (3.24)$$

4. Results

4.1. Sieve reactor

The topology-optimized candidates for the sieve reactor configuration obtained through the coupling of the pseudo model and the topology optimization algorithm are depicted in Fig. 9. Interestingly, for most of the generated designs, no flow channels directly connecting inlet and outlet interfaces are obtained, but rather tentacular configurations emerged. In such a way, the optimal flow channel design allows for effective transport of the moist air to TCM regions in the reactor, with the moist air crossing such regions prior to exiting the reactor. This is a unique result compared to the existing literature on the optimal FC design in energy devices and derives from the relatively small mass transfer resistance characterizing the porous TCM regions. In fact, for design cases presenting stronger mass transfer resistance in the second distributed material, FC networks connecting inlet and outlet interfaces are typically obtained [21,48].

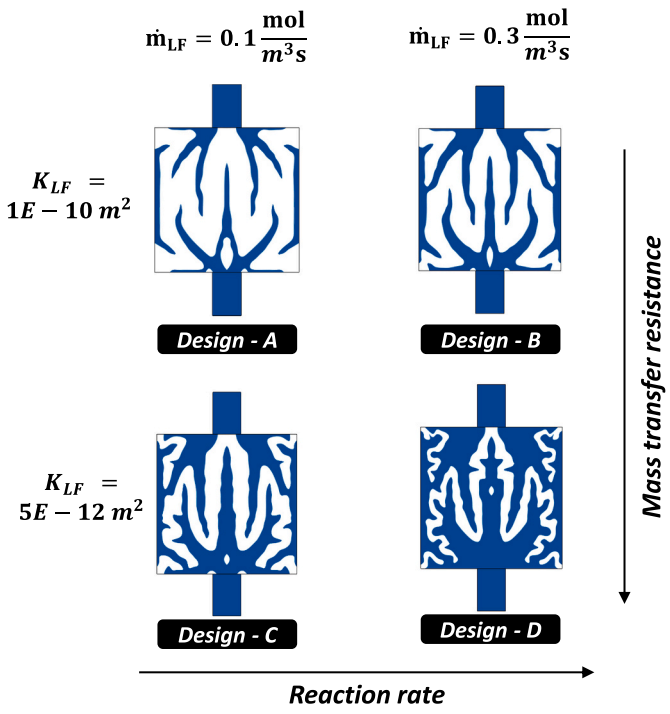

Fig. 9. Topology optimization-based designs for the sieve reactor configuration. The blue domain refers to the FC geometry, while the white domain refers to the TCM. (For interpretation of the references to color in this figure legend, the reader is referred to the web version of this article.)

Thicker channels are obtained in case of increased TCM permeability, i.e. larger K_{LF}. This makes intuitive sense, as the larger permeability values entail lower mass transfer resistance, with the moist air able to cross thicker TCM regions in case of a fixed pressure drop. Besides, the flow channel thickness also increases in the case of larger reaction rate. In fact, larger $\dot{m}_{LF}$ values entail higher rates at which water vapour is consumed, ultimately precluding the vapour transport in thick TCM regions. As a result, relatively small TCM content is obtained in e.g. design-D, while a large TCM over reactor volume ratio is achieved in the instance of design-A.

The packing factor values for each generated design candidate and the selected benchmark are reported in Table 3. Overall, lower packing factor values are achieved for lower reaction rates and higher permeability.

4.1.1. Performance assessment

In this section, the performance of the generated designs is compared with the selected literature benchmark. Firstly, the benefit led by the proposed design approach is evaluated by the comparison of the reactor energy density histories in Fig. 10 (a). Concerning the energy discharged at the desired discharge time, t^*, all the proposed designs are predicted to outperform the selected benchmark. In particular, an increase in the amount of discharged energy up to +76.4 % is obtained by the use of Design-B, leading to a capacity of 45.2 kWh for the single reactor module. This design presents a packing factor of 0.4, in close agreement with the selected benchmark design.

Design-B is also found as the most performing design for most of the simulated discharging time. However, if larger discharge times are considered, e.g. t = 300 h, Design-A is predicted as the most suitable design. This is due to the lower volume dedicated to the flow channels in the reactor (packing factor of 0.28), which ultimately increases the amount of storage material. That is, the optimal packing factor reduces with the desired discharge time. Nonetheless, this result indicates that the most performing design depends on the selected discharge time and that the variation of the seedings parameters can be used to obtain suitable designs depending on the selected discharge time.

The discharged exergy histories are reported in Fig. 10 (b). Differently from the discharged energy performance metrics, design-B is predicted here as the most performing design. This is an interesting result, demonstrating that the optimal geometrical features depend on the targeted performance metric. Thinner and shorter channels are thus predicted as the most efficient solution to maximize the discharged exergy. Besides, a small discrepancy is predicted between the benchmark design and designs-C and design-D. This result is dictated by the low mass transfer resistance for the generated TO candidates and, thus, larger mass flow rate, which in turn entails a limited temperature lift, as shown in Fig. 10 (c). The larger temperature lift is predicted for design-

Table 3
Packing factor for each generated design candidate and benchmark design [18].

	Design-A	Design-B	Design-C	Design-D	Benchmark
PF	0.28	0.40	0.53	0.68	0.43

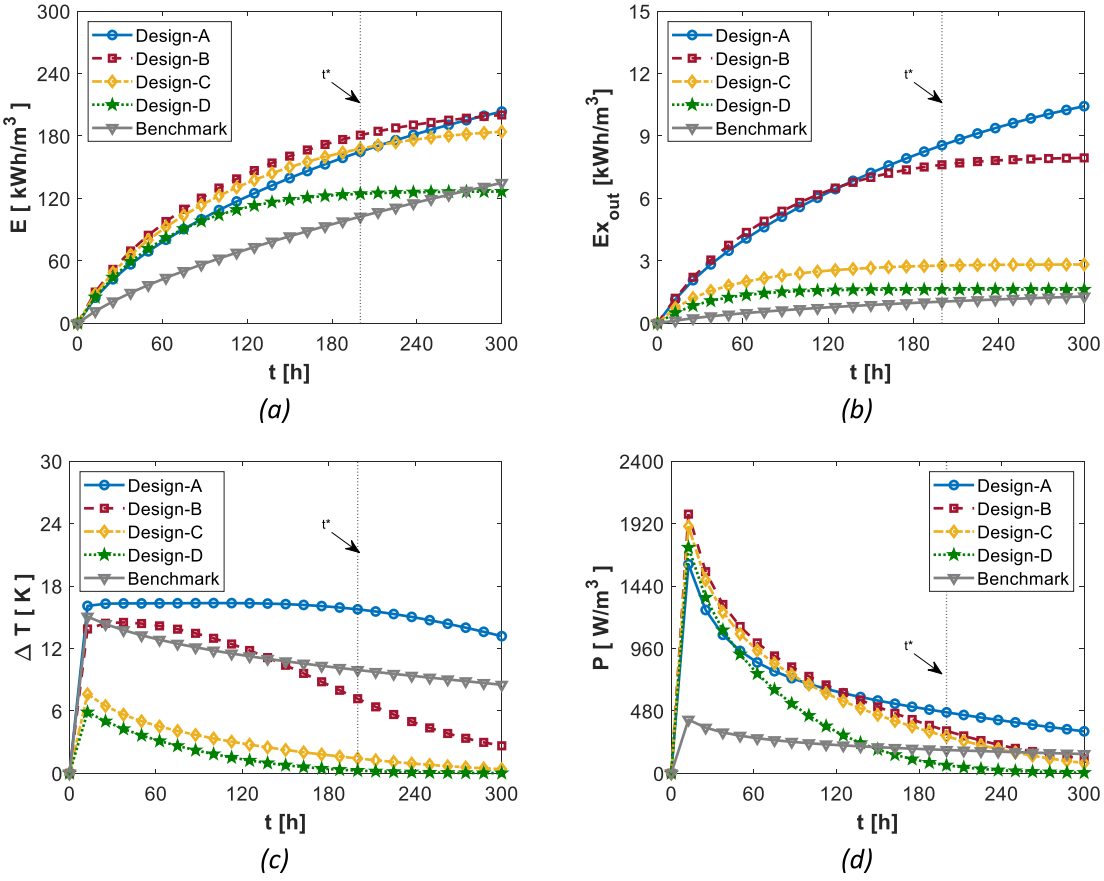

Fig. 10. Performance indicator histories comparison for the topology-optimized candidates in the sieve reactor configuration and benchmark design [18]: (a) Reactor energy density; (b) Exergy efficiency; (c) temperature lift; (c) Power output.

A, but only a mild enhancement is observed compared to the benchmark.

Different trends are instead observed for the reactor power output histories, depicted in Fig. 10 (d). A fairly steady history is predicted in the instance of the benchmark design, as was also suggested by the more linear energy discharge trend of Fig. 10 (a). The topology-optimized candidates all present a pronounced peak of power output during the initial steps of the hydration process. Such behaviour derives from the large velocity field values characterizing all the generated designs compared to the benchmark, with up to a 10 times increase in the predicted outlet velocity. The largest peak of power output value pertains again to design-B, which provides a performance enhancement of +383.0 % compared to the literature benchmark. As a result, the proposed optimization approach can also be adopted to generate high-power density reactors. That is also, the tentacular geometrical features observed in Fig. 9 are always advised for such an aim. On the other hand, alternative design paths must be followed in design cases pursuing a high power output steadiness [49].

The performance metrics values at the selected desired discharge time, t^*, are summarized in Table 4. As mentioned, the most suitable design depends on the targeted performance metric. However, the use of tentacular flow channels characterizing design-A and design-B is always recommended to enhance the mass transfer in the reactive bed, as higher performance metric values are always obtained compared to the selected benchmark.

Table 4
performance metrics values calculated considering a desired discharge time of 200 h.

PI	Design-A	Design-B	Design-C	Design-D	Benchmark
E_{t^*} [kWh/m^3]	164.9	<u>180.8</u>	167.8	124.4	102.5
Ex_{out,t^*} [kWh/m^3]	<u>8.6</u>	7.6	2.8	1.6	1.0
ΔT_{t^*} [K]	<u>16.1</u>	12.0	3.8	2.3	12.0
P_{peak} [W/m^3]	1607.8	<u>1992.5</u>	1898.9	1736.2	412.5

Fig. 11 shows the reaction advancement, temperature, airflow pressure and water vapour concentration contours at different time steps. The design-B and the benchmark design are compared. The TCM location in the benchmark design allows for good utilization of the first blocks of storage material, but a poor or null utilization is achieved for the blocks near the outlet interface due to the poor mass transfer in these regions. On the other hand, the generated FC geometry in design-B allows for a fairly homogeneous reaction advancement distribution, particularly in the proximity of the tentacular geometry elongating from the inlet interface. Relatively poor material utilization is still achieved for the TCM regions at the top of the reactor, which are thus found to react in longer times, $t > t^*$. Superior performance could likely be achieved by optimization approaches accounting for the complete physics interpretation and for time-dependent analysis.

Overall, no sharp transitions are predicted for the temperature distributions. The temperature in the TCM regions is higher than in the corresponding flow channels, as the reduced mass transfer resistance provides a more efficient cooling effect in the latter. A sharp transition is present in the airflow pressure contours and is dictated by the poor porous medium permeability of the hydrated salt. Limited influence from reaction rate is predicted here, as the airflow pressure contours do not vary with time. Similarly to the reaction advancement, the water vapour concentration contours, Fig. 11 (d), are predicted in design-B to propagate from the inlet flow channel boundaries towards the disconnected flow channel segments. A milder progression for the water

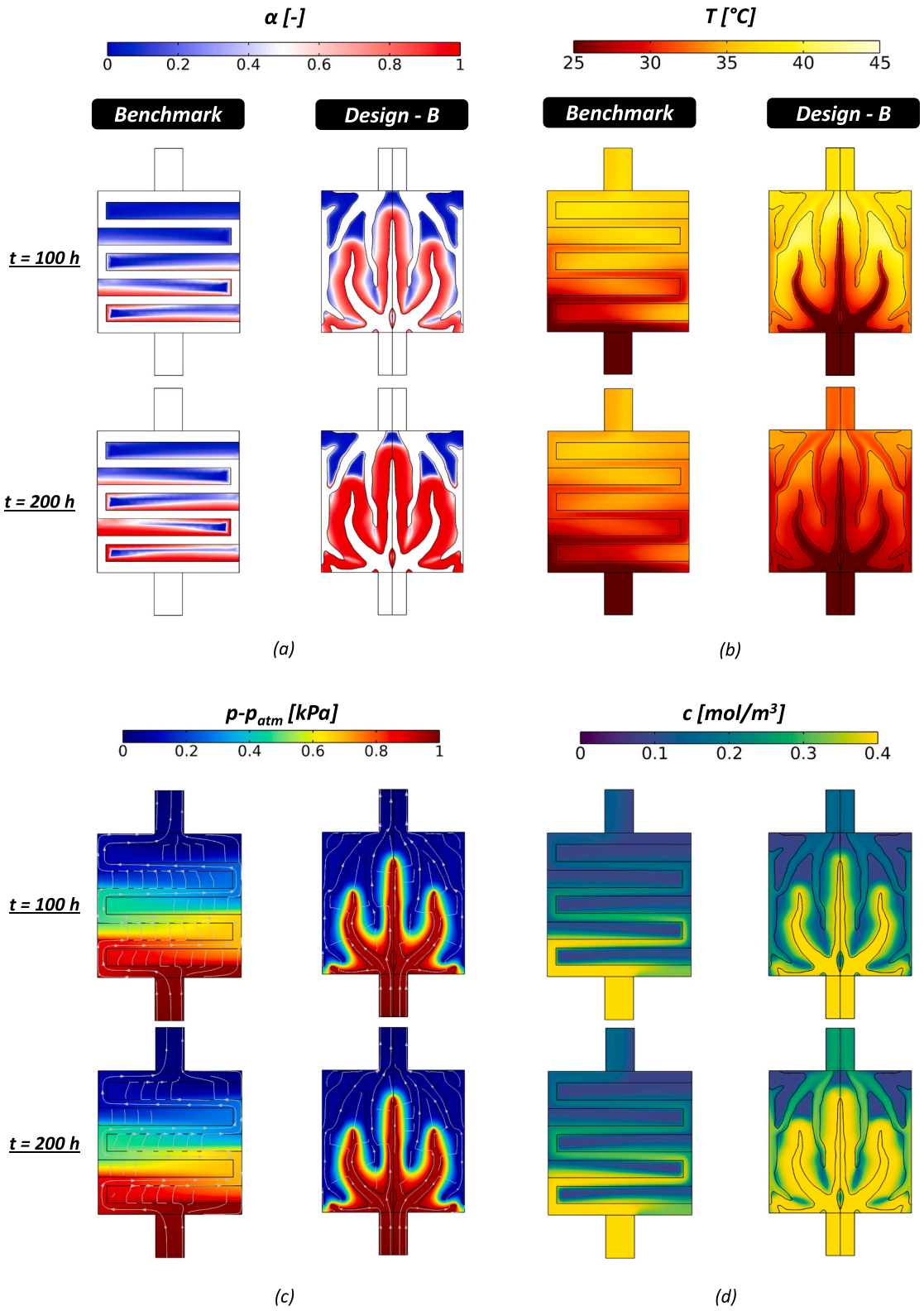

Fig. 11. Contour plots for design-B and benchmark design [18] at different time-steps: (a) reaction advancement, (b) temperature, (c) relative pressure and (d) water concentration.

vapour concentration distribution in the TCM regions is predicted for the benchmark design due to the poor mass flow rate crossing the porous medium.

4.2. Cylindrical reactor

The TO-design candidates generated in the instance of cylindrical reactors are shown in Fig. 12. The designs are depicted exploiting the axial symmetry with three-quarters of the obtained geometry shown to

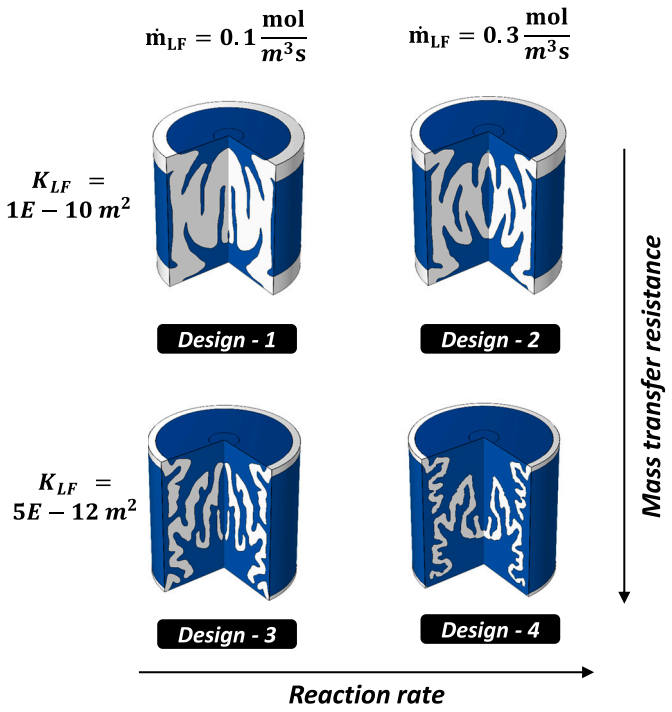

Fig. 12. Topology optimization-based designs for the cylindrical reactor configuration. The blue domain refers to the FC geometry, while the white domain refers to the TCM. (For interpretation of the references to color in this figure legend, the reader is referred to the web version of this article.)

present the optimized flow channel geometries. Similarly to sieve reactors, the optimized flow channels do not directly connect inlet and outlet interfaces but aim to distribute reactants in various TCM regions. Also, the same effect of the seeding parameter value on the generated designs is observed, with thicker and longer channels obtained for increasing mass transfer resistance and reaction rate. For some of the generated designs, e.g. design-2, flow channel segments disconnected from inlet and outlet interfaces emerged. These regions create preferential paths for the airflow directed to unreacted TCM before exiting the reactor, thus benefiting the reactants' transfer. These segments complicate the fabrication of the proposed designs. However, while examples of topology optimization problems considering manufacturability constraints have already been reported in the literature, e.g. [50], the manufacturability of these channel segments is beyond the scope of this paper.

The packing factor values for each generated design candidate and the selected benchmark are reported in Table 5. The TO designs all present a larger packing factor than the literature benchmark. This larger PF value derives from placing flow channels near the outer shell, and the ability of these flow channels to retrieve more thermal energy from the reactive bed is assessed in the next section.

4.2.1. Performance assessment

Fig. 13 shows the performance indicators for the generated design candidates and the benchmark design. Concerning the amount of energy discharged, only a slight variation is predicted among the four TO-design candidates. In the instance of the selected t^*, design-2 is predicted as the nondominated solution, with an increase in the amount of discharged energy up to +757.8 % compared to the selected benchmark design. A thermal capacity of 14.6 kWh was predicted for the single cylindrical module adopting the optimized flow channels. Design-2 presents a packing factor of 0.41, thus similar to the best-performing solution identified in the context of sieve reactors in Section 4.1.1. The nondominated design was generated by adopting the same seeding parameter values as for design-B. That is, large reaction rates and low mass transfer resistance values appear as the most indicated seeding parameters to generate high-performing TCS devices.

Concerning the discharged exergy, Fig. 13 (b), large performance discrepancies are obtained for the TO-design candidates. The designs presenting larger packing factors, i.e. design-3 and design-4, are predicted to lead to a low amount of discharged exergy. This result is dictated by the poor temperature lift, as shown in Fig. 13 (c). In fact, thick and long flow channel geometries guarantee a large mass flow rate in the reactive bed and promote cooling. As a result, while fast hydration rates are achieved, a poor airflow temperature increase is obtained. Overall, these results highlight the importance of selecting a relatively low packing factor to achieve higher discharged exergy values.

Interestingly, after an initial spike, the temperature lift from design-1 is predicted to increase with the discharging time slightly. For example, the temperature lift increases by 0.38 °C from 100 h to 200 h. The geometrical features dictate this trend. The reaction front initially propagates from the diffuser channel connected to the inlet interface. When the reaction front intercepts different diffuser channel segments, the gas reactants are transferred to unreacted regions which are activated and thus begin to contribute to the airflow temperature increase. This trend was not observed in the design candidates for sieve reactors due to the smaller distance between channel segments. However, the results obtained in this work are insufficient to derive design guidelines on maximising the temperature lift steadiness in time, although they demonstrate that the flow channel design can alter the temperature lift history from a TCS reactor.

Design-2 also results as a nondominated solution in maximising the peak of power output. This result derives from the large temperature output and the larger mass flow rate compared to design-1. Interestingly, despite a poor temperature lift, design-4 is predicted to provide a large peak of thermal power output. This is due to the large packing factor adopted, which ultimately ensures a limited mass transfer resistance in the TCS device and, thus, a large mass flow rate.

The performance metrics values for the selected desired discharge time, t*, are summarized in Table 6. Similarly to sieve reactors, the most suitable design varies with the targeted performance metric. Nevertheless, non-heuristic flow channels with low packing factors are recommended to enhance the mass transfer in the reactive bed. Overall, the predicted performance metrics values are lower than in sieve reactors. Considering the nondominated solutions from both investigated configurations, using sieve reactors ensures a +21.8 % increase in the amount of discharged energy and +215.0 % in discharged exergy.

Fig. 14 depicts the reaction advancement, temperature, airflow pressure and water vapour concentration contours at different time steps. Design-2 and the benchmark design are compared here. In the latter, poor material utilization is predicted due to the poor mass transfer achieved with the straight diffuser configuration. In fact, using a central pipe does not provide sufficient reactants distribution near the outer shell of the cylindrical reactor, ultimately preventing the discharge of a large fraction of the storage material. Concerning design-2, the reaction front propagates in time from the boundary of the flow channel connected to the inlet interface. Besides, at time-step 200 h, the reaction front is predicted to propagate also from the disconnected flow channel segments. In fact, the presence of hydrated material between the inlet channel and these segments allows for gas reactants in the latter. As a result, regions of unreacted materials away from the inlet interface can be activated.

Table 5
Packing factor for each generated design candidate and benchmark design in the instance of cylindrical reactor configuration.

	Design-1	Design-2	Design-3	Design-4	Benchmark
PF	0.27	0.41	0.57	0.69	0.04

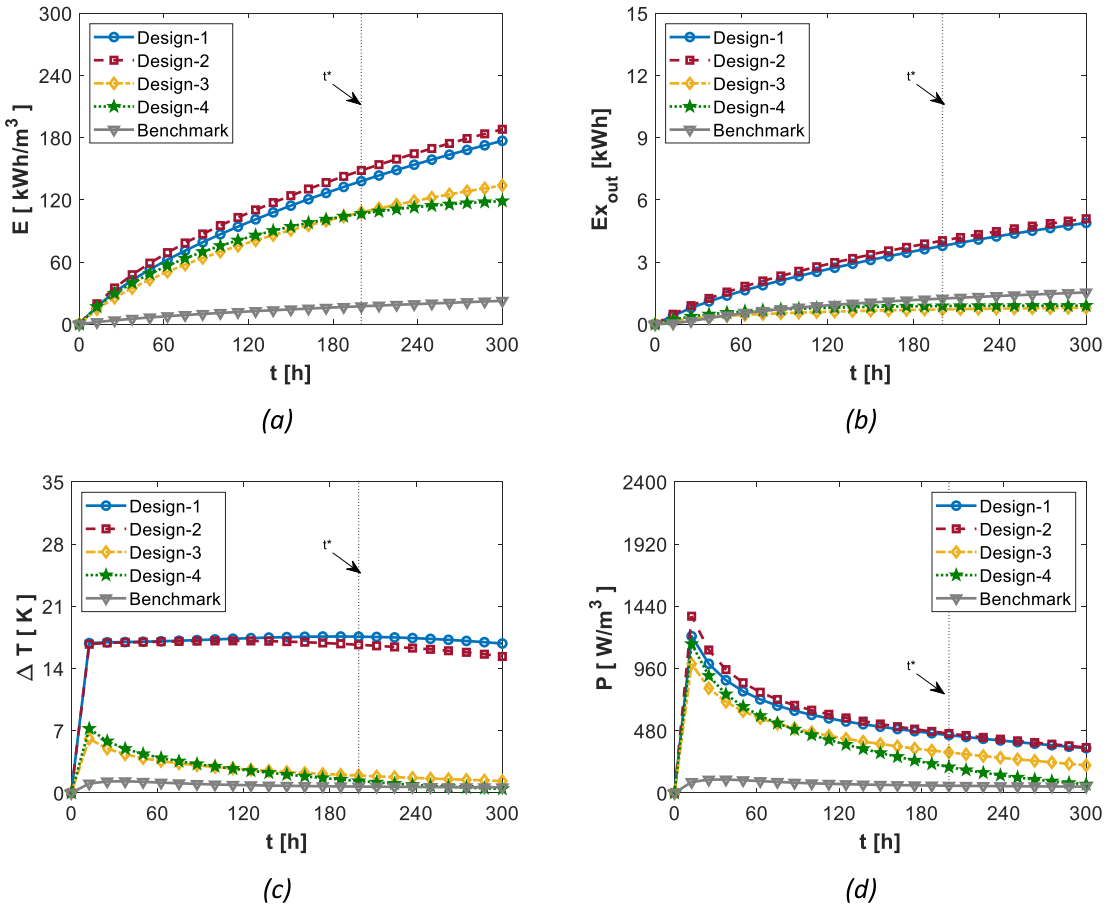

Fig. 13. Performance indicator histories comparison of topology-optimized candidates in the cylindrical reactor configuration and benchmark design [11]: (a) Reactor energy density; (b) Exergy efficiency; (c) temperature lift; (c) Power output.

Table 6
Performance metrics values calculated considering a desired discharge time, t*, of 200 h.

PI	Design-1	Design-2	Design-3	Design-4	Benchmark
E_{t^*} [kWh/m^3]	138.1	148.4	107.9	106.7	17.3
Ex_{out,t^*} [kWh/m^3]	3.8	4.0	0.7	0.9	1.2
ΔT_{t^*} [K]	17.1	16.9	3.3	3.5	1
P_{peak} [W/m^3]	1209.1	1363.5	995.7	1149.4	103.8

5. Considerations on the design fabrication

This section discusses possible manufacturing routes for the optimal designs presented in the study. The complex geometrical emerging from the adopted optimization approach might indeed complicate the fabrication of the proposed reactors. Three-dimensional representations of two of the generated design candidates are depicted in Fig. 15. Concerning the sieve configuration, the design was obtained through the extrusion of the optimized flow channel geometries, while the cylindrical design was obtained through the revolution of the flow channel geometry around the central tube axis. The flow channel boundaries are made of a perforated metallic structure, which allows for the transfer of the carrier fluid (moist air) and, at the same time, ensures structural support for the storage material.

Additive Manufacturing (AM) can be used to fabricate the flow channel designs. AM has many advantages over conventional manufacturing routes and has been increasingly used in a vast number of applications [51]. The flexibility of additive manufacturing to fabricate complex geometries from polymer and ferrous materials [52] presents unique opportunities for innovative design concepts. Additive manufacturing is, thus, an enabling technology that allows designers to overcome the current manufacturing limitation that inhibits the adoption of topology optimization as a design tool. In recent years, additive manufacturing of topologically optimized energy devices has been growing rapidly [51,53], as several successful examples have been reported in the literature. For instance, Li et al. [54] manufactured and tested TO-based cooling channels to mitigate thermal hotspot effects in electronic components. Compared to a conventional parallel design, larger heat transfer capabilities were measured for the optimized designs, with a maximum surface temperature reduction of −11.7 %. Similarly, in the field of thermal management of batteries, Mo et al. [55] adopted AM to fabricate TO-based cooling channels made in $AlSi_{10}Mg$ material. In the context of thermal energy storage, Ge et al. [56] demonstrated the use of selective laser melting additive manufacturing as a manufacturing route for directly fabricating a TO-based design of a multi-tube shell-and-tube latent heat thermal energy storage device.

However, AM is still an emerging technique, while conventional manufacturing methods such as machining and injection molding/casting still dominate the manufacturing sector [57,58]. Consequently, a second possible manufacturing route is envisioned based on the use of TO-inspired designs. The emerging geometrical features can be post-processed and simplified into '*conventional*' geometrical objects, such as straight channels. In this way, a trade-off between improved performance and manufacturability can be achieved. An example of this solution was provided in the work by Pizzolato et al. [40], where a binary skeleton was obtained through sequential thinning of the topology optimization results. Line segments were used to generate a straight skeleton with enhanced manufacturability compared to the original TO-

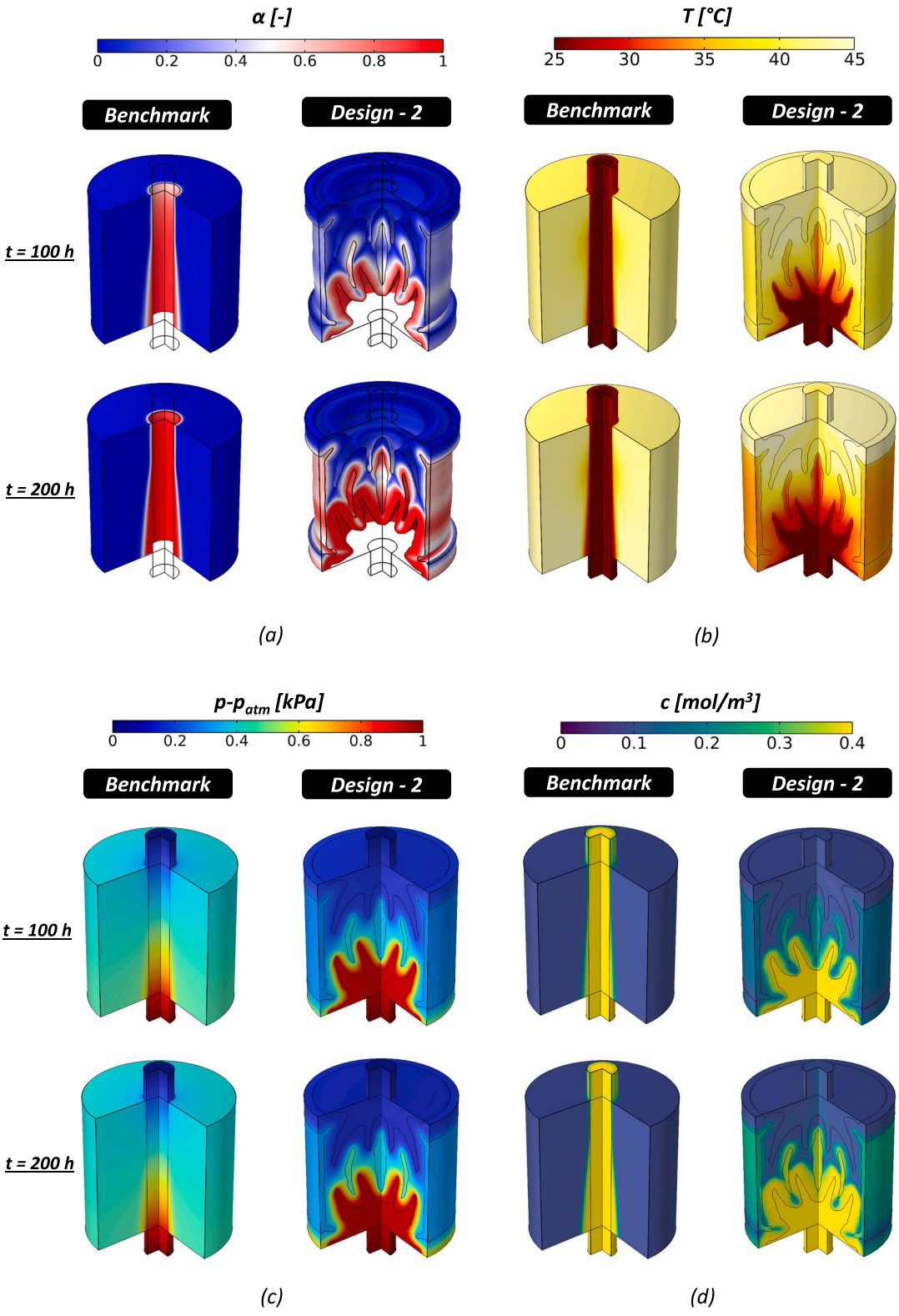

Fig. 14. Contour plots for design-B and benchmark design [11] at different time-steps: (a) reaction advancement, (b) temperature, (c) relative pressure and (d) water concentration.

design, with the thickness selected to match specific packing factor requirements. In the near future, we envision this second manufacturing route as the preferred one to limit the investment cost linked to the reactor design. Nonetheless, it is crucial to stress that the optimization approach proposed in this work is necessary to identify non-intuitive geometrical features which can greatly benefit performance and ultimately generate manufacturable and high-performing reactors.

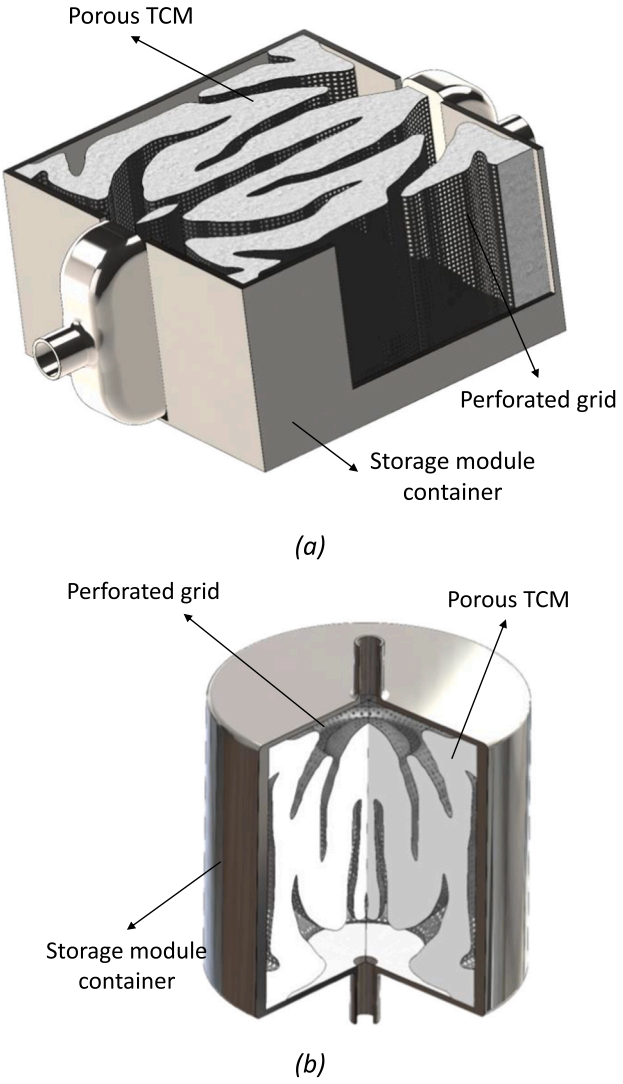

Fig. 15. 3D representation of two of the generated designs: (a) design-B and (b) design-1.

6. Considerations on limitations and future works in topological optimization for open TCS reactors

This section analyzes the limitations of the proposed design approach and suggests potential future research areas. The reactor design proposed in this work specifically targeted open TCS reactors operated for domestic heating applications. The performance assessment exhibited these designs to significantly outperform current literature solutions, thus demonstrating the benefits deriving from the use of topology optimization algorithm in the technological framework under analysis. Therefore, we believe the present study to constitute an initial platform upon which future TO research could be based. In this regard, this section highlights potential areas for further research work:

- *Experimental validation*: Primary efforts need to be placed on the validation of the optimization results reported in this work. Overall, the scientific community is still sceptical regarding the engineering outcomes of the topology optimization approach. To ultimately overcome this scepticism, experimental evidence is necessary to fully demonstrate the benefits led by non-heuristic design tools. In the experimental assessment of these devices, it is crucial to connect the analysis to conventional designs to quantify and discuss the advantages.
- *Application scenarios*: this work considered specific conditions selected to replicate the integration of a TCS reactor in domestic heating applications. Nevertheless, given the increasing number of applications of TCS systems [59], future research could be devoted to exploring the optimal design of TCS reactors for applications different from the one considered in this work. Examples of these scenarios are short-term energy storage and high-temperature energy storage.
- *Methodological framework*: Future research could focus on modifying and expanding the capabilities of pseudo model representing the targeted physical problem. Efforts need to be placed on implementing time-dependent models to capture the dynamic behaviour of TCS devices. Nonetheless, it is relevant to stress that the methodological approach adopted in this work can be easily extended to other energy devices. The use of topology optimization for the performance enhancement of energy devices is often hampered by the challenges of coupling the full physical description with the topology optimization algorithm. By means of the multi-step TO approach, insights on the performance enhancement of energy devices can be derived from the optimization of simplified cases re-evaluated through more accurate numerical models. This design pathway can rely on topology optimization problems which are established in the literature and already available from commercial software. That is, little efforts need to be made by research to couple the TO algorithm to the desired analysis model. In the instance of well-approximated problems, the non-intuitive TO-based designs can enhance the performance of the existing devices and lead to technological advancements. This route is a rapid way to increase energy efficiency, which is key to achieving the decarbonisation goals set for future energy scenarios.
- *Operating conditions and TCM selection*: The proposed designs were generated and assessed under specific operating conditions and for specific desired discharge times. The design trends that emerged for these conditions have been extensively discussed in this work. Nonetheless, as highlighted in previous research studies [3,60], the behaviour of TCS systems depends on the considered boundary conditions, such as inlet temperature, inlet vapour pressure and pressure drop. Consequently, future work could be directed to elucidate how these choices influence the optimal design of a TCS reactor. Similarly, the effect of the TCM selection on the optimality of a design could be investigated. A link between optimal geometrical features and reaction kinetics could benefit the TCS community.
- *TCS reactor dimensions*: specific reactor dimensions were selected in this work, with the rationale for these choices discussed in Section 2. Nonetheless, these dimensions can vary with the intended application for the TCS reactor, and a comprehensive analysis of the effect of the reactor dimensions on the optimal geometrical features and packing factor is recommended.

7. Conclusions

This work addresses the need for mass transfer enhancement in open system TCS reactors. A multi-step topology optimization approach was proposed to generate and assess a series of non-heuristic flow channel designs. Such designs aimed to effectively distribute a gas reactant in the reactive sites. From the results presented in this work, the following main conclusions can be derived:

- The proposed topology optimization approach constitutes an affordable and thorough design tool for the non-heuristic configuration of open system TCS reactors. The performance of the generated designs is predicted to lead to an enhancement of up to +757.8 % in the amount of discharged energy compared to state-of-the-art solutions;
- The generated designs present tentacular flow channels which do not directly connect inlet and outlet interfaces. These flow channel

geometries favour the transport of gas reactants in regions away from the inlet interface as well as the transport of the collected heat towards the outlet interface.

- The geometrical features for the most suitable design differ depending on the selected performance metrics. For example, thinner and shorter flow channels favour the maximization of the amount of exergy gained from the HTF compared to the amount of energy. Nevertheless, tentacular flow channel geometries are predicted to outperform benchmark designs regardless of the considered performance metric.
- Concerning the nondominated solutions identified in this work, rectangular reactors outperform cylindrical reactors. An increased amount of discharged energy up to +21.8 % is predicted. Thus, sieve reactors employing non-heuristic flow channel geometries are identified as the most-performing geometrical configuration for open system TCS devices.

Ultimately, the results and design framework presented in this work can largely impact the development of TCS devices and the evidence presented establishes new enhancement pathways in the context of open system TCS reactors.

CRediT authorship contribution statement

Gabriele Humbert: Conceptualization, Methodology, Investigation, Software, Formal analysis, Writing - original draft, Writing - review & editing, Visualization. Adriano Sciacovelli: Conceptualization, Methodology, Formal Analysis, Management, Writing - review & editing, Resources, Project administration, Funding acquisition.

Declaration of competing interest

The authors declare that they have no known competing financial interests or personal relationships that could have appeared to influence the work reported in this paper.

Data availability

Data will be made available on request.

Acknowledgments

The authors would like to acknowledge the financial support from the Engineering and Physical Sciences Research Council (EPSRC), United Kingdom (EP/R016402/1).

References

[1] IRENA, Innovation Outlook Thermal Energy Storage, 2020.
[2] L. Scapino, H.A. Zondag, J. Van Bael, J. Diriken, C.C.M. Rindt, Sorption heat storage for long-term low-temperature applications: a review on the advancements at material and prototype scale, Appl. Energy 190 (2017) 920–948, https://doi.org/10.1016/j.apenergy.2016.12.148.
[3] B. Michel, N. Mazet, P. Neveu, Experimental investigation of an innovative thermochemical process operating with a hydrate salt and moist air for thermal storage of solar energy: global performance, Appl. Energy 129 (2014) 177–186, https://doi.org/10.1016/j.apenergy.2014.04.073.
[4] H. Liu, W. Wang, Y. Zhang, Performance gap between thermochemical energy storage systems based on salt hydrates and materials, J. Clean. Prod. 313 (2021), 127908, https://doi.org/10.1016/j.jclepro.2021.127908.
[5] R.J. Clark, A. Mehrabadi, M. Farid, State of the art on salt hydrate thermochemical energy storage systems for use in building applications, J. Energy Storage 27 (2020), 101145, https://doi.org/10.1016/j.est.2019.101145.
[6] D. Aydin, S.P. Casey, S. Riffat, The latest advancements on thermochemical heat storage systems, Renew. Sust. Energ. Rev. 41 (2015) 356–367, https://doi.org/10.1016/j.rser.2014.08.054.
[7] M. Gaeini, H.A. Zondag, C.C.M. Rindt, Effect of kinetics on the thermal performance of a sorption heat storage reactor, Appl. Therm. Eng. 102 (2016) 520–531, https://doi.org/10.1016/j.applthermaleng.2016.03.055.
[8] C.J. Ferchaud, H.A. Zondag, A. Rubino, R. De Boer, Seasonal sorption heat storage – research on thermochemical materials and storage performance, in: Proc Heat Power Cycle 2012, 2012, pp. 1–7.
[9] N. Vahedi, A. Oztekin, Split flow modified packed bed reactor for cobalt oxide based high-temperature TCES systems, in: ASME Int. Mech. Eng. Congr. Expo. Proc vol. 6, American Society of Mechanical Engineers (ASME), 2019, https://doi.org/10.1115/IMECE2019-10740.
[10] F. Dorai, M. Rolland, A. Wachs, M. Marcoux, E. Climent, Packing fixed bed reactors with cylinders: influence of particle length distribution, Procedia Eng. 42 (2012) 1335–1345, https://doi.org/10.1016/J.PROENG.2012.07.525.
[11] D. Aydin, S.P. Casey, X. Chen, S. Riffat, Novel, "open-sorption pipe" reactor for solar thermal energy storage, Energy Convers. Manag. 121 (2016) 321–334, https://doi.org/10.1016/j.enconman.2016.05.045.
[12] B. Michel, N. Mazet, S. Mauran, D. Stitou, J. Xu, Thermochemical process for seasonal storage of solar energy: characterization and modeling of a high density reactive bed, Energy 47 (2012) 553–563, https://doi.org/10.1016/j.energy.2012.09.029.
[13] A. Krönauer, E. Lävemann, S. Brückner, A. Hauer, Mobile sorption heat storage in industrial waste heat recovery, Energy Procedia 73 (2015) 272–280, https://doi.org/10.1016/j.egypro.2015.07.688.
[14] R. Van Alebeek, L. Scapino, M.A.J.M. Beving, M. Gaeini, C.C.M. Rindt, H. A. Zondag, Investigation of a household-scale open sorption energy storage system based on the zeolite 13X/water reacting pair, Appl. Therm. Eng. 139 (2018) 325–333, https://doi.org/10.1016/j.applthermaleng.2018.04.092.
[15] W. Li, H. Guo, M. Zeng, Q. Wang, Performance of SrBr 2·6H2O based seasonal thermochemical heat storage in a novel multilayered sieve reactor, Energy Convers. Manag. 198 (2019), 111843, https://doi.org/10.1016/j.enconman.2019.111843.
[16] A. Malley-Ernewein, S. Lorente, Constructal design of thermochemical energy storage, Int. J. Heat Mass Transf. 130 (2019) 1299–1306, https://doi.org/10.1016/j.ijheatmasstransfer.2018.10.097.
[17] A. Bejan, The constructal law of organization in nature: tree-shaped flows and body size, J. Exp. Biol. 208 (2005) 1677–1686, https://doi.org/10.1242/jeb.01487.
[18] A.A. Hawwash, H. Hassan, Feky K. El, Impact of reactor design on the thermal energy storage of thermochemical materials, Appl. Therm. Eng. 168 (2020), 114776, https://doi.org/10.1016/J.APPLTHERMALENG.2019.114776.
[19] W. Chen, W. Li, Y. Zhang, Analysis of thermal deposition of MgCl2·6H2O hydrated salt in the sieve-plate reactor for heat storage, Appl. Therm. Eng. 135 (2018) 95–108, https://doi.org/10.1016/j.applthermaleng.2018.02.043.
[20] M. Bendsoe, O. Sigmund, Topology Optimization: Theory, Methods, And Applications, Springer, Berlin Heidelberg, 2004, https://doi.org/10.1007/978-3-662-05086-6.
[21] K. Yaji, S. Yamasaki, S. Tsushima, T. Suzuki, K. Fujita, Topology optimization for the design of flow fields in a redox flow battery, Struct. Multidiscip. Optim. 57 (2018) 535–546, https://doi.org/10.1007/s00158-017-1763-8.
[22] K. Yaji, S. Yamasaki, K. Fujita, Data-driven multifidelity topology design using a deep generative model: application to forced convection heat transfer problems, Comput. Methods Appl. Mech. Eng. 388 (2022), 114284, https://doi.org/10.1016/J.CMA.2021.114284.
[23] K. Yaji, S. Yamasaki, K. Fujita, Multifidelity design guided by topology optimization, Struct. Multidiscip. Optim. 61 (2019) 1071–1085, https://doi.org/10.1007/s00158-019-02406-4.
[24] B. Michel, P. Neveu, N. Mazet, Comparison of closed and open thermochemical processes, for long-term thermal energy storage applications, Energy 72 (2014) 702–716, https://doi.org/10.1016/j.energy.2014.05.097.
[25] A. Malley-Ernewein, S. Lorente, Analysis of thermochemical energy storage in an elemental configuration, Sci. Rep. 9 (2019) 15875, https://doi.org/10.1038/s41598-019-52249-8.
[26] R. Fisher, Y. Ding, A. Sciacovelli, Hydration kinetics of K2CO3, MgCl2 and vermiculite-based composites in view of low-temperature thermochemical energy storage, J. Energy Storage (2021) 38, https://doi.org/10.1016/j.est.2021.102561.
[27] K.E. N'Tsoukpoe, T. Schmidt, H.U. Rammelberg, B.A. Watts, W.K.L. Ruck, A systematic multi-step screening of numerous salt hydrates for low temperature thermochemical energy storage, Appl. Energy 124 (2014) 1–16, https://doi.org/10.1016/j.apenergy.2014.02.053.
[28] J. Stengler, I. Bürger, M. Linder, Thermodynamic and kinetic investigations of the SrBr 2 hydration and dehydration reactions for thermochemical energy storage and heat transformation, Appl. Energy 277 (2020), 115432, https://doi.org/10.1016/j.apenergy.2020.115432.
[29] D. Gilles, T. Segato, E. Courbon, M. Degrez, P. D'Ans, Affordable process for the production of strontium bromide used in low grade heat recovery applications, Procedia CIRP 69 (2018) 383–388, https://doi.org/10.1016/J.PROCIR.2017.11.056.
[30] A. Fopah-Lele, J.G. Tamba, A review on the use of SrBr 2·6H2O as a potential material for low temperature energy storage systems and building applications, Sol. Energy Mater. Sol. Cells 164 (2017) 175–187, https://doi.org/10.1016/j.solmat.2017.02.018.
[31] F. Okkels, H. Bruus, Scaling behavior of optimally structured catalytic microfluidic reactors, Phys. Rev. E Stat. Nonlinear Soft Matter Phys. 75 (2007) 2–5, https://doi.org/10.1103/PhysRevE.75.016301.
[32] A. Gersborg-Hansen, O. Sigmund, R.B. Haber, Topology optimization of channel flow problems, Struct. Multidiscip. Optim. 30 (2005) 181–192, https://doi.org/10.1007/s00158-004-0508-7.
[33] J. Alexandersen, C.S. Andreasen, A review of topology optimisation for fluid-based problems, Fluids 5 (2020) 1–33, https://doi.org/10.3390/fluids5010029.

[34] J. Alexandersen, N. Aage, C.S. Andreasen, O. Sigmund, Topology optimisation for natural convection problems, Int. J. Numer. Methods Fluids 76 (2014) 699–721, https://doi.org/10.1002/FLD.3954.
[35] M. Gaeini, R. Wind, P.A.J. Donkers, H.A. Zondag, C.C.M. Rindt, Development of a validated 2D model for flow, moisture and heat transport in a packed bed reactor using MRI experiment and a lab-scale reactor setup, Int. J. Heat Mass Transf. 113 (2017) 1116–1129, https://doi.org/10.1016/j.ijheatmasstransfer.2017.06.034.
[36] S. Mauran, H. Lahmidi, V. Goetz, Solar heating and cooling by a thermochemical process. First experiments of a prototype storing 60 kW h by a solid/gas reaction, Sol. Energy 82 (2008) 623–636, https://doi.org/10.1016/j.solener.2008.01.002.
[37] A. Fopah-Lele, C. Rohde, K. Neumann, T. Tietjen, T. Rönnebeck, K.E. N'Tsoukpoe, et al., Lab-scale experiment of a closed thermochemical heat storage system including honeycomb heat exchanger, Energy 114 (2016) 225–238, https://doi.org/10.1016/j.energy.2016.08.009.
[38] COMSOL - Software for Multiphysics Simulation. https://www.comsol.com/, 2020 (accessed November 15, 2021).
[39] G. Humbert, Y. Ding, A. Sciacovelli, Combined enhancement of thermal and chemical performance of closed thermochemical energy storage system by optimized tree-like heat exchanger structures, Appl. Energy 311 (2022), 118633, https://doi.org/10.1016/J.APENERGY.2022.118633.
[40] A. Pizzolato, A. Sharma, K. Maute, A. Sciacovelli, V. Verda, Design of effective fins for fast PCM melting and solidification in shell-and-tube latent heat thermal energy storage through topology optimization, Appl. Energy 208 (2017) 1–18, https://doi.org/10.1016/j.apenergy.2017.10.050.
[41] T. Borrvall, J. Petersson, Topology optimization of fluids in stokes flow, Int. J. Numer. Methods Fluids 41 (2003) 77–107, https://doi.org/10.1002/fld.426.
[42] K. Svanberg, MMA and GCMMA-two methods for nonlinear optimization. https://people.kth.se/~krille/mmagcmma.pdf, 2007 (accessed May 12, 2020).
[43] K. Maute, E. Ramm, Adaptive topology optimization, Struct. Optim. 10 (1995) 100–112, https://doi.org/10.1007/BF01743537.
[44] L.F. Cabeza, E. Galindo, C. Prieto, C. Barreneche, Fernández A. Inés, Key performance indicators in thermal energy storage: survey and assessment, Renew. Energy 83 (2015) 820–827, https://doi.org/10.1016/j.renene.2015.05.019.
[45] M.J. Moran, H.N. Shapiro, D.D. Boettner, M.B. Bailey, Fundamentals of Engineering Thermodynamics, 1987.
[46] Y. Pahamli, M.J. Hosseini, S.S. Ardahaie, A.A. Ranjbar, Improvement of a phase change heat storage system by Blossom-Shaped Fins: energy analysis, Renew. Energy 182 (2022) 192–215, https://doi.org/10.1016/J.RENENE.2021.09.128.
[47] M.T. Luu, D. Milani, M. Nomvar, A. Abbas, A design protocol for enhanced discharge exergy in phase change material heat battery, Appl. Energy (2020) 265, https://doi.org/10.1016/J.APENERGY.2020.114801.
[48] R. Behrou, A. Pizzolato, A. Forner-Cuenca, Topology optimization as a powerful tool to design advanced PEMFCs flow fields, Int. J. Heat Mass Transf. 135 (2019) 72–92, https://doi.org/10.1016/j.ijheatmasstransfer.2019.01.050.
[49] A. Pizzolato, A. Sharma, K. Maute, A. Sciacovelli, V. Verda, Topology optimization for heat transfer enhancement in Latent Heat Thermal Energy Storage, Int. J. Heat Mass Transf. 113 (2017) 875–888, https://doi.org/10.1016/j.ijheatmasstransfer.2017.05.098.
[50] L. Harzheim, G. Graf, A review of optimization of cast parts using topology optimization, Struct. Multidiscip. Optim. 31 (2005) 388–399, https://doi.org/10.1007/S00158-005-0554-9.
[51] L. Meng, W. Zhang, D. Quan, G. Shi, L. Tang, Y. Hou, et al., From topology optimization design to additive manufacturing: today's success and tomorrow's roadmap, Arch. Comput. Meth. Eng. 27 (2020) 805–830, https://doi.org/10.1007/s11831-019-09331-1.
[52] T. Pham, P. Kwon, S. Foster, Additive manufacturing and topology optimization of magnetic materials for electrical machines—a review, Energies 14 (2021) 1–24, https://doi.org/10.3390/en14020283.
[53] J.R. McDonough, A perspective on the current and future roles of additive manufacturing in process engineering, with an emphasis on heat transfer, Therm. Sci. Eng. Prog. 19 (2020), 100594, https://doi.org/10.1016/j.tsep.2020.100594.
[54] H. Li, X. Ding, F. Meng, D. Jing, M. Xiong, Optimal design and thermal modelling for liquid-cooled heat sink based on multi-objective topology optimization: an experimental and numerical study, Int. J. Heat Mass Transf. 144 (2019), 118638, https://doi.org/10.1016/J.IJHEATMASSTRANSFER.2019.118638.
[55] X. Mo, H. Zhi, Y. Xiao, H. Hua, L. He, Topology optimization of cooling plates for battery thermal management, Int. J. Heat Mass Transf. 178 (2021), 121612, https://doi.org/10.1016/J.IJHEATMASSTRANSFER.2021.121612.
[56] R. Ge, G. Humbert, R. Martinez, M.M. Attallah, A. Sciacovelli, Additive manufacturing of a topology-optimised multi-tube energy storage device: experimental tests and numerical analysis, Appl. Therm. Eng. 180 (2020), 115878, https://doi.org/10.1016/j.applthermaleng.2020.115878.
[57] J. Liu, Y. Ma, A survey of manufacturing oriented topology optimization methods, Adv. Eng. Softw. 100 (2016) 161–175, https://doi.org/10.1016/j.advengsoft.2016.07.017.
[58] D. Thomas, Costs, benefits, and adoption of additive manufacturing: a supply chain perspective, Int. J. Adv. Manuf. Technol. 85 (2016) 1857–1876, https://doi.org/10.1007/s00170-015-7973-6.
[59] E. Borri, G. Zsembinszki, L.F. Cabeza, Recent developments of thermal energy storage applications in the built environment: a bibliometric analysis and systematic review, Appl. Therm. Eng. 189 (2021), 116666, https://doi.org/10.1016/j.applthermaleng.2021.116666.
[60] V. Palomba, S. Vasta, A. Freni, Experimental testing of AQSOA FAM Z02/water adsorption system for heat and cold storage, Appl. Therm. Eng. 124 (2017) 967–974, https://doi.org/10.1016/j.applthermaleng.2017.06.085.